In-situ Synthesis of SERS Active Au@POM Nanostructures in a Microfluidic Device for Real Time Detection of Water Pollutants

Marta Lafuente,[†, ‡] Ismael Pellejero,[§] Alberto Clemente,[†,‡,§] Miguel A. Urbiztondo,[‖] Reyes Mallada,[†,‡,⊥] Santiago Reinoso,*[§] María P. Pina,*[†,‡,⊥] Luis M. Gandía[§]

[†]Nanoscience Institute of Aragon (INA), University of Zaragoza, Department of Chemical & Environmental Engineering, Edificio I+D+i, Campus Rio Ebro, C/Mariano Esquillor s/n, 50018 Zaragoza, Spain

[‡]Instituto de Ciencia de Materiales de Aragón (ICMA), Universidad de Zaragoza-CSIC, 50009 Zaragoza, Spain.

[§]Institute for Advanced Materials and Mathematics (InaMat[2]), Universidad Pública de Navarra (UPNA), Edificio Jerónimo de Ayanz, Campus de Arrosadia, 31006 Pamplona, Spain.

[‖]Centro Universitario de la Defensa de Zaragoza, Carretera Huesca s/n, 50090 Zaragoza, Spain.

[⊥]Networking Research Center on Bioengineering, Biomaterials and Nanomedicine, CIBER-BBN, 28029 Madrid, Spain.

ABSTRACT: We present a simple, versatile and low-cost approach for the preparation of SERS-active regions within a microfluidic channel 50 cm in length. The approach involves the UV-light-driven formation of polyoxometalate-decorated gold nanostructures, Au@POM (POM: $H_3PW_{12}O_{40}$ (PW) and $H_3PMo_{12}O_{40}$ (PMo)), that self-assemble in situ on the surface of the PDMS microchannels without any extra functionalization procedure. The fabricated LoCs were characterized by SEM, UV-Vis, Raman, XRD and XPS techniques. The SERS activity of the resulting Au@POM–coated lab-on-a-chip (LoC) devices was evaluated in both static and flow conditions using Rhodamine R6G. The SERS response of Au@PW–based LoCs was found superior to Au@PMo counterparts and outstanding when compared to reported data on metal@POM nanocomposites. We demonstrate the potentialities of both Au@POM–coated LoCs as analytical platforms for real time detection of the organophosphorous pesticide Paraoxon-methyl at 10^{-6} M concentration level.

INTRODUCTION

Surface Enhanced Raman Spectroscopy (SERS) is one of the current leading techniques for the ultrasensitive detection of organic molecules. SERS combines the high specificity of Raman scattering with the signal amplification provided by the excitation of surface plasmon resonances in metallic nanostructures (electromagnetic enhancement), together with the charge transfer mechanisms established between analytes and metal surfaces (chemical enhancement).[1-2] One crucial aspect for prompting results is the stability and homogeneity of large scale SERS-active substrates. Au^0 surfaces, with superior thermal and chemical stability, are the most extensively explored in this area over the more affordable Cu^0 [3-4] and Ag^0 surfaces with higher SERS activity.[5-7]

Metal ions such as Au^{III}, Ag^I, Pd^{II} or Pt^{IV} are known to reduce easily to colloidal metal nanoparticles (NPs) through light-driven reactions, under mild conditions, with polyoxometalates (POMs) acting as photocatalysts.[8-10] POMs are photoactive metal-oxygen anionic clusters that behave as electron reservoirs thanks to their ability to undergo fast, reversible and multi-step proton-coupled redox processes upon excitation with UV radiation, without experiencing any substantial structural impact. These features make POMs ideal vehicles for the synthesis of well-dispersed metal NPs, playing the role of both, reducing agents and stabilizers of the resulting metal nanostructures. Thanks to the formation of an outer protective shell of oxidized clusters, further aggregation processes are prevented. Unlike for the most commonly used protective ligands (i.e. citrate, phosphate, thiolates), POM-stabilized colloidal metal NPs exhibit unique reactivity, thus increasing the scope for their effective application in a wide range of fields including photo- and electro-catalysis, liquid-phase oxidation, biosensing, energy storage and medicine.[11-12] In comparison, the SERS activity of metal@POM hybrid nanostructures has

remained largely unexplored. Some representative examples are: the morphologically diverse Ag^0 dendrites stabilized by PW clusters that were assembled by Liu *et al.* on Al surfaces through a galvanic displacement process;[13] the collection of composites made of bimetallic NPs prepared by Bansal and co-workers through galvanic replacement on colloidal TiO$_2$ impregnated with PW;[14] the hexagonal 2D arrays of densely packed Au^0 NPs obtained by Lai et al. within the channels of a mesostructured PW-silicatropic template;[15] and Baruah and Miller's colloidal Au^0 NPs prepared by partial replacement of capping citrate ligands with decavanadate clusters.[16]

The scarcity of SERS studies dealing with POMs based heterostructures is somehow surprising when considering the fact that, compared to other plasmonic metal surfaces, such metal@POM nanostructures can offer remarkable advantages arising from synergistic effects between the plasmonic metal cores (i.e. local electromagnetic field intensification) and the metal-oxygen cluster shells due to the electronic characteristics and energy levels of the latter (i.e. charge transfer mechanism). For example, Baruah and Miller attributed the moderate improvement of the SERS signal by ca. one order of magnitude exhibited by their decavanadate-capped colloidal Au^0 NPs to the adjunctive chemical enhancement of the stabilizing POM shell.[16]

In this study, the exceptional characteristics of SERS, the potentialities of metal@POM hybrid nanostructures and the advantages of microfluidic technology are combined for the first time to be employed efficiently in SERS applications. The so-called Lab on a Chip (LoC) SERS systems benefit from the ultrasensitivity provided by SERS while reducing the required sample volume thanks to the LoC. These advantages are at the origin of LoC-SERS devices becoming a hot topic in the field of chemical and biological sensing.[17-19] In this context, innovative fabrication protocols for the integration of SERS substrates into microfluidic chips have been developed in the past few years. These protocols include: the sputtering and patterning of noble-metal films on

Si nanopillars manufactured by oxygen-plasma-stripping of photoresists;[20] the femtosecond laser direct writing of Ag^0 microflower arrays within glass microchannels;[21] the aerosol jet printing with Au^0 NP inks of polystyrene-based microfluidic channels obtained from roll-to-roll hot embossing;[22] or the remote metal writing of Au^0 nanopatterns within glass-fabricated microfluidic channels by two-photon lithography.[23] In all of them, expensive instrumentation and intricate fabrication steps are involved. On the contrary, this work presents a simple, versatile and low cost approach towards the reproducible fabrication of large SERS-active regions in a microfluidic PDMS chip. Soft lithography is among the most relevant techniques for fabricating microfluidic systems due to the ease of manufacture and low in capital cost by replica molding again elastomeric or rigid molds. Nowadays, molds can be easily fabricated with good replica resolution by 3D printing. In fact, this emerging technology contributes even more to the expansion of microfluidic chips thanks to its well-known characteristics such as versatility, accessibility and low cost.[24-26] These features, together with the excellent optical (transparency above 240 nm) and mechanical (elasticity) properties of polydimethylsiloxane (PDMS), make microfluidic PDMS platforms ideal for novel SERS developments.[27-29]

The first part of this work is devoted to the LoC fabrication and the "in situ" functionalization with SERS active nanostructures based on Au@POM composites. The influence of the POM cluster on the NP size, surface coverage and plasmonic properties of the Au@POM coatings is extensively investigated by SEM, XRD, XPS, UV-Vis, and Raman techniques. In the second part, the SERS activity of the resulting LoC-SERS devices is evaluated in both static and flow conditions using Rhodamine R6G as probe molecule. Finally, the performance for real time detection of Paraoxon-methyl pesticide is characterized, with special emphasis on SERS response recovery for reusability purposes. Finally, their application for the continuous

monitoring of the Paraoxon-methyl pesticide, as illustrative example of emerging contaminant, is demonstrated.

EXPERIMENTAL SECTION

Materials

The following materials were purchased from commercial sources and used as received: Sylgard 184 silicone elastomer from Dowsil, $HAuCl_4 \cdot 3H_2O$ from Merck ($\geq$ 99.9%), $H_3PW_{12}O_{40}$ hydrate from Sigma-Aldrich (ACS reagent), $H_3PMo_{12}O_{40}$ hydrate from Sigma-Aldrich (ACS reagent), Propan-2-ol from Scharlau (99.5%), Rhodamine 6G from Sigma-Aldrich (99%) and Paraoxon-methyl (Dimethyl 4-nitrophenyl phosphate) purchased as analytical standard from Sigma-Aldrich.

Fabrication of PDMS Microfluidic Chips

The PDMS-based microfluidic chips were fabricated by polymer casting over 3D-printed molds. The method followed in this work was reported previously in the literature,[30] but has been slightly modified to our end (Figure 1a). A serpentine-shaped model with semicircular section (diameter 1 mm, depth 500 μm, total volume 210 mm^3) was designed by using the computer-aided design software AutoCAD$^®$. The negative mold of such design was fabricated by 3D printing stereolithography with a B9Creator V1.2 high-resolution 3D printer using B9R-6 resin (B9Creations). The as-fabricated 3D mold was carefully washed with propan-2-ol, dried and baked in an oven at 160 °C for 1 h in order to remove any rest of the precursor resin. The PDMS polymer solution, consisting in a mixture of Sylgard 184 silicone-based elastomer and curing agent (w/w = 10:1), was poured on the 3D-printed master mold. The casted mold was fully outgassed under vacuum and cured in an oven at 80 °C for 30 min. Afterwards, the PDMS replica was peeled off from the master mold and attached to a PDMS-fabricated flat cover by

using corona plasma treatment (BD-20AC Electro-Technic Products) for 30 s over both pieces, which were then pressed together and baked again at 80 °C for 1 h. A standard cover glass (Labbox CCVN-020-100, thickness of 0.15 mm) was glued on the top cover to enable the SERS measurements. Finally, Nordson EDF microfluidic connections were inserted on the inlet/outlet ports. All the PDMS microfluidic chips displayed a thickness of ca. 5 mm and a footprint of 4×4 cm^2, thus making such chip design a very compact system.
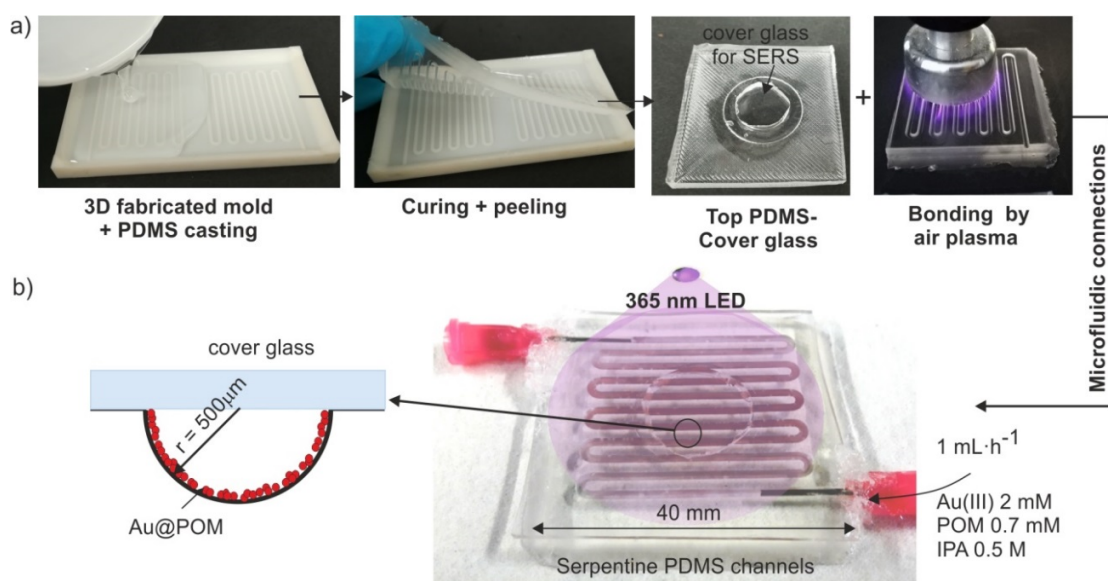
Figure 1. (a) 3D-printing-assisted fabrication procedure of PDMS microfluidic chips. (b) Direct UV-light-driven synthesis of Au@POM nanostructures inside the PDMS channels.

In-situ Synthesis of Au@POM Nanostructures

The photo-assisted synthesis of hybrid Au@POM nanostructures was carried out directly inside the channels of the PDMS microfluidic chips as illustrated in Figure 1b. The experimental set-up is shown in Figure S1 in the Supporting Information. Firstly, stock solutions of HAuCl$_4$ (2 mM), H$_3$PW$_{12}$O$_{40}$ denoted as PW (0.7 mM) and H$_3$PMo$_{12}$O$_{40}$ denoted as PMo (0.7 mM) dissolved in aqueous 0.5 M propan-2-ol were prepared. Then, equal volumes of the HAuCl$_4$ and

the corresponding POM solutions were mixed together, deoxygenated by bubbling Ar for 5 min, and injected by a syringe pump through the PDMS microchannels at a rate of 1 mL·h^{-1}. These experimental conditions were defined on the basis of previous results not shown here. The PMo and PW species have been selected to explore how the type of addenda metal (Mo^{VI} vs W^{VI}) affects the POM performance and the SERS activity of the LoC devices.

To induce the in situ formation of the Au@POM nanostructures, the precursor solution passing through the microchannel was irradiated with UV light for 2 h (reaction time). For this purpose, a 365 nm UV LED lamp (LZ1-00UV00–Led Engin, 1.2 W illumination flux) was centered over the PDMS chip at a distance of 25 mm to provide 4.5 mW·cm^{-2} of irradiance. Such coatings were characterized by SEM (FEI Quanta scanning electron microscope), UV-Vis absorbance (Varian Cary 50 UV-Vis spectrometer), XRD (Bruker D8 Advance High Resolution Diffractometer) and XPS (Kratos Axis X-ray spectrometer). Particle size was determined from statistical analysis of SEM images by using the processing software ImageJ. In addition, the NPs collected in the outlet solution were characterized by UV-Vis absorbance (Flame Ocean Optics spectrophotometer) and STEM (FEI Tecnai F30 transmission electron microscope), respectively.

SERS Experiments

SERS measurements were carried out in a WITec Alpha 300 Raman spectrometer equipped with a confocal optical microscope (480 nm as lateral spatial resolution). All the spectra were recorded at room temperature with an excitation wavelength of $\lambda = 785$ nm and optical lens of ×20. Such conditions were the resulting from a previous screening in order to optimize the Raman signal. The Au@POM–coated PDMS microfluidic chips were mounted in the experimental set-up displayed in Figure S2 in the Supporting Information. Both parameters, the

laser power and acquisition time were finely tuned depending on the sample (Table S1 in the Supporting Information).

The analytical enhancement factor (AEF), also denoted as SERS Gain, quantifies the increase of signal intensity that can be expected from SERS as compared to normal Raman spectroscopy under given experimental conditions, and is calculated with Equation 1:

$$AEF = \frac{I_{SERS}/(t_{SERS} \times P_{SERS} \times c_{SERS})}{I_{Raman}/(t_{Raman} \times P_{Raman} \times c_{Raman})} \qquad \text{Equation 1}$$

Where C_{Raman} and C_{SERS} are the R6G concentration in the Raman (1 mM) and SERS (1 µM) measurements conditions, respectively; I_{Raman} and I_{SERS} are the intensity values of the R6G characteristic band at 1510 cm^{-1}, corresponding to the stretching vibration of the C–C bonds, for the normal Raman and SERS measurements, respectively. Similarly, P_{Raman}, t_{Raman} and $P_{SERS,}$ t_{SERS} refer to the laser power and acquisition time values for the normal Raman and SERS measurements, respectively. The normal Raman R6G spectrum was measured focusing the laser beam inside the stock solution 1×10^{-3} M of R6G. Thus, I_{Raman} corresponds to the intensity of the R6G molecules measured in liquid phase. For SERS measurements, a R6G solution 1×10^{-6} M was pumped through the microfluidic device for 1 hour; then, the chip was flushed with distilled water. Thus, I_{SERS} is the intensity of the R6G molecules that remain adsorbed on the SERS substrate. The real time detection experiments of Paraoxon-methyl were carried out for an aqueous solution 1×10^{-6} M pumped at 0.5 mL·min^{-1} through the microfluidic device.

RESULTS AND DISCUSSION

Fabrication and Characterization of Au@POM-Coated PDMS Microfluidic Chips

The direct synthesis of Au@POM nanostructures inside the PDMS microchannels was carried out by irradiation with UV light of a continuous flow of an aqueous mixture of Au^{III}, the corresponding POM and propan-2-ol (see Figure 2). In this process, the POM plays the roles of:

i) transferring electrons from the sacrificial electron-donor propan-2-ol to the Au^{III} atoms through photo-induced redox cycles; ii) stabilizing the Au^0 NP cores generated in situ by forming a POM shell; and iii) hampering aggregation by electrostatic repulsion between protective POM shells. Two different $H_3PM_{12}O_{40}$ commercial POMs have been studied in this work: PW ($M = W^{VI}$) and PMo ($M = Mo^{VI}$). Both show the α-Keggin-type structure, in which four trimers of three edge-sharing MO_6 octahedra each arrange in ideal T_d symmetry around a central XO_4 tetrahedron (X = P) by sharing vertices (Figure S3 in the Supporting Information).
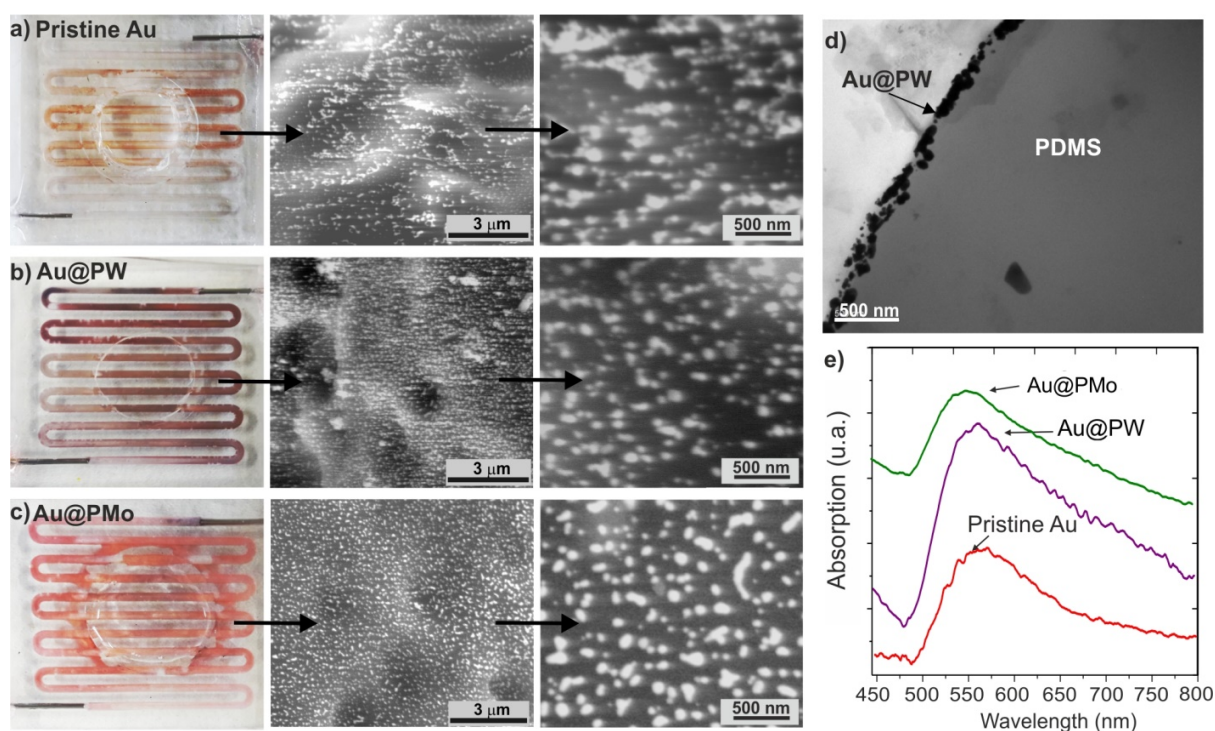

Figure 2. Optical and SEM images of the PDMS chips coated with: (a) pristine Au^0; (b) Au@PW nanostructures; (c) Au@PMo nanostructures; (d) HRTEM cross-section of Au@PW nanostructures. (e) UV-Vis absorbance spectra of the Au nanostructures on the PDMS surfaces.

Although the XPS measurements give only a semiquantitative elemental composition, the presence of C, O, W/Mo and Au elements in the coatings was confirmed (see Figure 3). The

calculated atomic ratio Au/Mo and Au/W accounts for 5.5 and 7.3, respectively. The two characteristic Mo 3d peaks (232.9 and 236 eV) of the pristine $H_3PMo_{12}O_{40}$, corresponding to the Mo^{VI} oxidation state, remain in the Au@PMo nanostructure. However, the W 4f peaks of the $H_3PW_{12}O_{40}$ (35.9 and 38.1 eV) are shifted towards higher binding energies in the Au@PW analogue. For both Au@POMs, the binding energy of the Au 4f signals 88.1 eV and 84.4 eV coincides with that for bulk gold, indicating that majority of the gold of the hybrid nanostructures is in a metallic state.[31] The O 1s core level spectra were fitted with two peaks at 530.5-531 eV ascribed to the Mo-O and W-O bonding present in POMs, and at higher binding energy of 531.5-532 eV related to –OH groups.[32] The contribution of these hydroxyl groups is largely diminished on pristine $H_3PMo_{12}O_{40}$ and $H_3PW_{12}O_{40}$ samples (see O1s XP spectra deconvolution in Figure S4 in the Supporting Information).

The XRD patterns of Au@POM coated chips clearly display the {111}, {200} and {220} Bragg reflections of face-centered cubic (fcc) of gold (Figure 4). As expected, the characteristic diffraction peaks of the protective POM shell, observed at 26.5º - 26.7º and 33.1º - 33.3º, appear highly attenuated. In addition, they do not coincide with those observed for the pristine POMs diffraction pattern. This observation is explained by considering the occurrence of a strong interaction POM-Au capable to introduce distortions within the POM tertiary structure.[33]
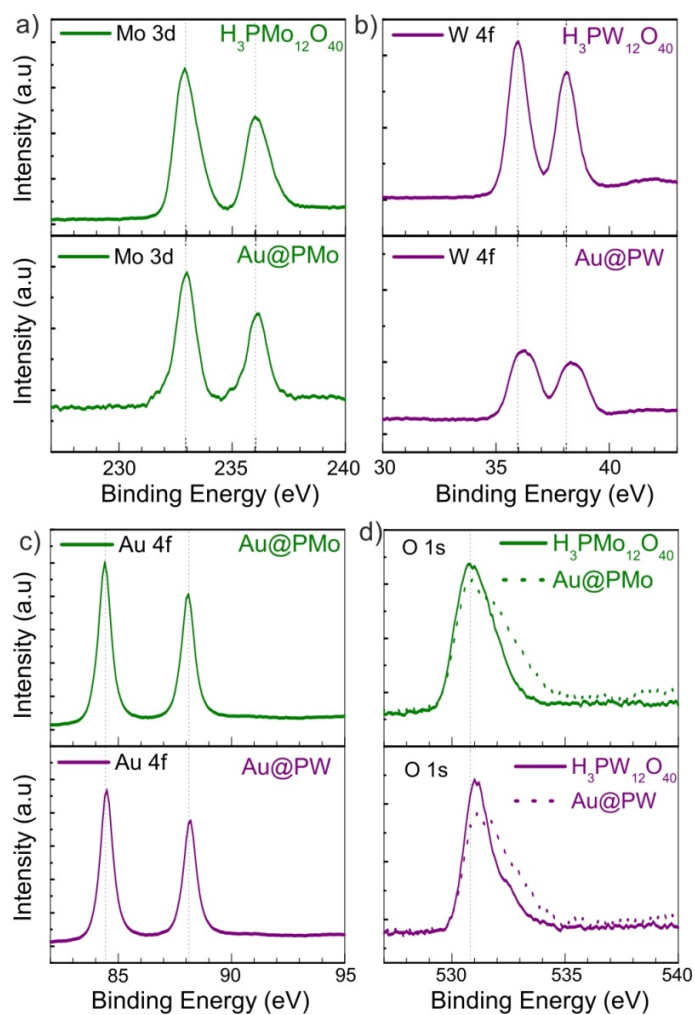
Figure 3. High resolution XP spectra of: a) Mo 3d; b) W 4f; c) Au 4f; d) O 1s.
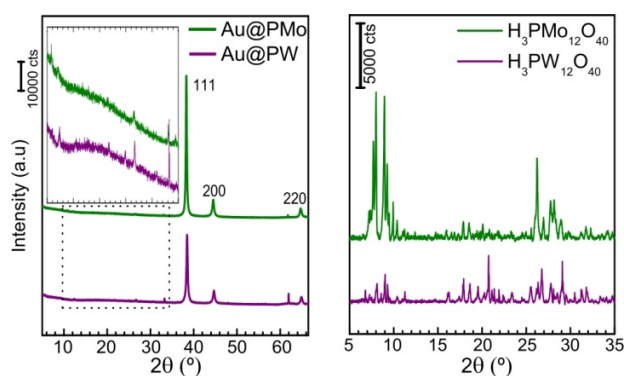
Figure 4. XRD pattern of Au@POM drop-coated films (left) and pristine POMs in powder form (right).

The reaction conditions, shown in Figure 1b, lead to a preferential synthesis of Au@POM nanostructures on the wall surface of the PDMS microchannels for both POMs. The SEM and STEM images displayed in Figure 2b and Figure 2c show how the Au@POM nanostructures are uniformly distributed along the serpentine channel. The surface coverage values have been calculated to range from 20 to 30% for both types of POMs. The SPR spectra (Figure 2e) of the Au@POM nanostructures assembled at the PDMS surface feature broad bands with maxima centered at 550–555 nm, which are consistent with the sizes of 100 ± 27 and 89 ± 20 nm estimated for the Au@PMo and Au@PW nanostructures, respectively. Therefore, the larger size of the Au^0 core in the Au@PMo nanostructures is attributed to the superior redox activity of the PMo cluster compared to the PW analogue.[34]

The preferential synthesis on the PDMS surface is supported by a nucleation-growing mechanism in which the roughness, i.e. 95 nm, and zeta potential[35] of the PDMS surface are promoting the heterogeneous nucleation of Au^0 seeds (Figure 2d). Such nuclei grow further in presence of POMs and remain attached to the microfluidic wall via electrostatic interactions due to reaction pH is below the isoelectric point of PDMS. The POM clusters are grafted at the naked surfaces of the Au^0 assemblies while forming, thus acting as protective capping ligands to lead to the final Au@POM nanostructures. To corroborate our hypothesis, similar experiments conducted in the absence of any POM cluster, led to Au^0 NPs but also aggregates on the PDMS surface. The presence of a significant amount of uncovered areas is clearly visible in the SEM images shown in Figure 2a. In addition, the naked Au^0 individual NPs were comparatively smaller in size and more polydisperse (65±21 nm) than the Au@POM nanostructures, leading to a less intense band centered at 575 nm in the SPR spectrum (Figure 2e). Indeed, the larger Au@POM surface coverage when compared to the naked-Au^0 counterpart is explained by the

strong acidity of the POMs.[36] In absence of POMs, the PDMS surface is negatively charged; and consequently, the heterogeneous nucleation is notably hindered. On the contrary, the addition of the POM clusters to the reaction mixture provokes the acid hydrolysis of the PDMS surface with the consequent increase of hydroxyl groups on the PDMS surface as XPS measurements shown (Figure 3d).

Although to a limited extent, homogeneous nucleation and growing also took place during UV irradiation, but only when the POM was present. Thus, a small fraction of colloidal Au@POM NPs was also collected from the outlet solution (Figure S5 in the Supporting Information). The analysis of the STEM images afforded comparable average sizes for the NPs synthesized with both POMs, the dimensions being ca. 29 ± 5 and 24 ± 6 nm for the Au@PMo and Au@PW colloids, respectively. The UV-Vis spectra of the colloidal NPs show intense absorption lines at 522 nm for PW and 535 nm for PMo, which are narrower than those observed for Au@POM coatings at 550–555 nm. This substantial blue-shift and narrowing is consistent with the presence of smaller and less polydispersed Au@POM moieties in the liquid phase.

SERS Activity of Au@POMMicrofluidic Devices

Figure 5 compares the SERS spectra of the Au@POM–coated chips and the Raman spectra of the pristine PW and PMo species at 785 nm laser wavelength. In general, the maximum SERS response of the as prepared nanostructures would be expected by using 532 nm as laser line.[37-38] However, in this work, the expected superior SERS performance at shorter wavelength laser has been sacrificed to prevent paraoxon-methyl photodegradation during the measurement.

The specific spectral signature for each POM, with the bands originating from stretching vibrations of analogous metal-oxygen bonds, is occurring at frequencies higher for the PW anion than for PMo. Thus, the lines at 995 and 975 cm^{-1} in the spectrum of the PMo species, as well as

those at 1010 and 988 cm^{-1} in the case of PW, are readily assigned to the symmetric and antisymmetric stretching vibrations of the M = O$_d$ bonds, respectively, where O$_d$ accounts for the double-bonded terminal O atoms.[39] In addition, the less intense bands at 931 and 889 cm^{-1} for PW, as well as at 906 cm^{-1} for PMo, are observed in the magnification inserts of Figure 5. These Raman signals are attributed to the antisymmetric stretching vibrations of the M-Ob-M bonds, where where O$_b$ accounts for the bridging O atoms between corner-sharing [MO$_6$] octahedral. The fact that the signal intensities found in the spectrum of PMo are significantly lower than those afforded by PW is fully consistent with the weaker polarization of the electron distribution determined for the former anion according to computational DFT-calculations.[34]

The spectra of the Au@POM–coated PDMS chips indicate that the primary Keggin structure remains intact in the hybrid nanostructures. However, the favored orientation of the POM cluster at the Au^0 surface induces a remarkable blue-shift and intensity enhancement for those signals located at ca. 890 cm^{-1} for the Au@PMo and at 957 cm^{-1} for Au@PW–coated chips. These lines are assigned to the v_{as}(Mo-O$_b$-Mo) and v_{as}(W-O$_b$-W) vibrational modes, respectively. Accordingly, we propose the grafting of Keggin-type anions to noble-metal NPs via O$_b$ chemisorption at the surface of the Au^0 cores in agreement with previous works.[40-41] In this configuration, the POM shell consists in a monolayer of clusters oriented with the four-fold symmetry axis perpendicular to the metal surface so as to maximize the metal−oxygen interactions. This hypothesis would also support the difractograms of the drop-casted Au@POM films shown in Figure 4.
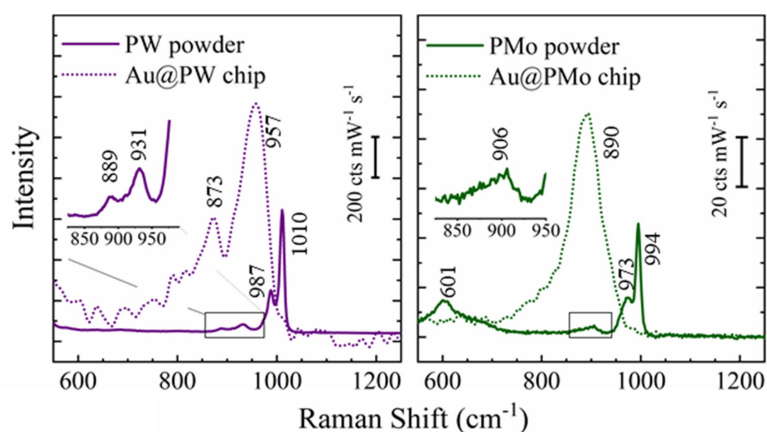
Figure 5. Raman spectra of the pristine PW (left) and PMo (right) POMs compared to the SERS spectra of the corresponding Au@POM–coated PDMS chips. Inserts: magnification of the Raman spectra of the pristine POMs in the 850-950 cm^{-1} region.

Figure 6 shows the comparison of the Raman spectrum of R6G as a bulk solid with the SERS spectra of an aqueous 1 µM R6G solution recorded for the chip with the pristine Au^0 coating and for the two Au@POM–coated chips. The SERS activities of the Au@POM–coated chips are both higher than that shown by the pristine Au^0 coating. Among the two POM coated chips, the SERS activity of the Au@PW substrate is outperforming when compared to that of the Au@PMo counterpart. This fact evidences that some compositional changes for a given POM framework with certain charge (Mo^{VI} versus W^{VI} in our case) can substantially modify the SERS response of morphologically comparable substrates.

The AEF of R6G[42] increases from 7.08×10^5 for the Au@PMo–coated chip up to 1.65×10^7 for the Au@PW analogue. This latter value also stands out as far superior to those reported for Au@POM hybrid nanostructures with the decavanadate $[V_{10}O_{28}]^{6-}$ cluster, among which a maximum 2.6×10^5 AEF of crystal violet at 633 nm is achieved for nanostructures 51 nm in size.[16] Above all, the as-prepared low cost the Au@PW devices exhibit a SERS gain, ~10^{-7},

similar to the ones shown by LoCs prepared following other more sophisticated approaches.[17] Finally, the AEF of Au[0]–coated chip is 1.24×10^5, in accordance with its low Au NPs surface coverage (Figure 2a) motivated by the hindered Au-PDMS interactions.
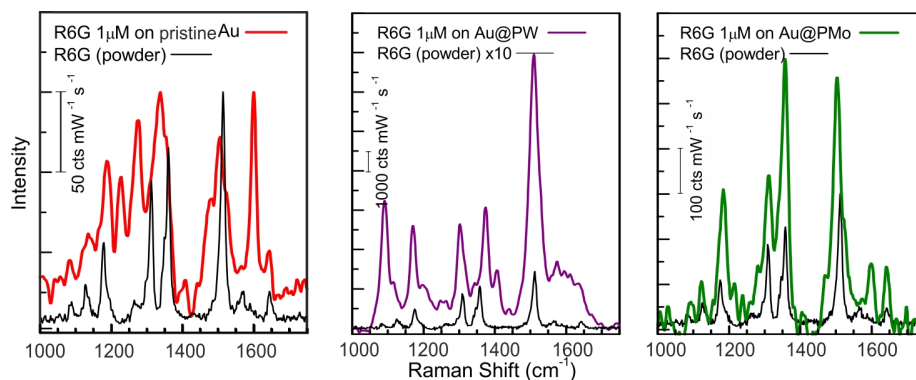
Figure 6. SERS spectra of 1 µM R6G solution acquired in static conditions for the PDMS chips coated with pristine Au[0] assemblies (left), Au@PW nanostructures (center), and Au@PMo nanostructures (right).

We hypothesize that the higher SERS activity found for the Au@PW–coated chip is mainly attributed to a more effective chemical coupling between the Au[0] NP cores and the PW clusters in the outer shell. The chemical enhancement mechanism, which can lead to EF values in the range from 10 to 10^2 depending on the nature of the probe molecule and its surface complex with the SERS-active substrate,[43] has been reported to be likely strong in molecules with significant stabilization of the HOMO–LUMO gap.[44] And this could be our case, because the HOMO–LUMO gap of the PW anion is significantly larger than that of the PMo analogous species according to DFT calculations (2.8 eV versus 2.03 eV).[34] Herein, it is worthy to mention that the laser we have used in our experiments (1.58 eV) cannot promote any resonance mechanism by producing photo-excited electrons and holes in the R6G molecule due to the band gap of the latter being 2.3 eV. Thus, the PW based system benefits from larger synergistic effects between

17

the Au^0 NPs, the protective POM shells and the target analyte, which provoke an efficient charge transfer from the Au^0 cores to the LUMO level of the PW ligands, and then to the LUMO level of the R6G molecules.

On line measurements with dye solutions were also carried out to evaluate performance of our large Au@POM SERS active regions in analyte capture. It is well known that surface selectivity is a key aspect in SERS detection as the enhancement effect only occurs in the very close vicinity of the metallic nanostructures. Thus, POMs with negatively charged oxo-enriched surfaces are likely to show high efficiency and selectivity towards the adsorption of organic dye molecules driven not only by electrostatic interactions between areas with positive and negative charge densities, but also by classical hydrogen bonding and weak C−H···O or M−O···π interactions.

To corroborate our hypothesis, an aqueous 1 µM R6G solution was continuously pumped at a rate of 0.5 mL·min^{-1} through the microfluidic chips. The SERS intensity of the main band of this cationic dye at 1516 cm^{-1}, used as reference, was constantly monitored while the R6G solution (detection) or distilled water (recovery) was pumping through the microfluidic channel during 5 consecutive on/off cycles of 10 min each. The reproducibility of the SERS response for Au@PMo coated device is illustrated in Figure 7a, where the average signal is plotted for each measuring cycle. The relative standard deviation (RSD) results analyzed at 100 random spots within the optical window were all below 20 %. The homogeneity of the SERS response along 1200 microns length of the central microfluidic channel is shown in Figure S6 of the Supporting Information for both Au@POM coated chips. Besides, a fast and reversible adsorption of the R6G probe dye was observed for at least five consecutive adsorption-desorption cycles,

throughout which the reference signal intensity displayed nearly full recovery in less than 6 min upon water flushing (Figure 7b).
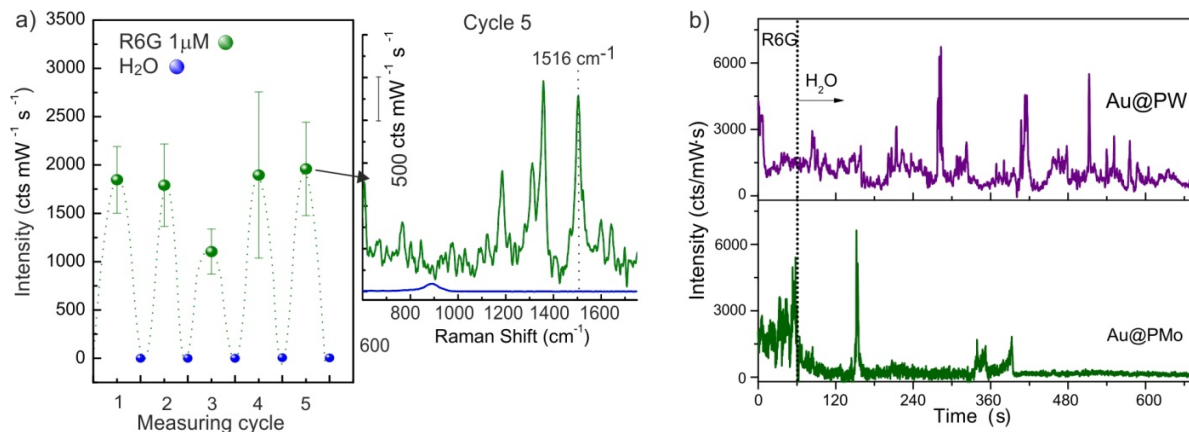
Figure 7. (a) Evolution of the Raman signal at 1516 cm^{-1} (average and standard deviation of 100 spectra) measured on the Au@PMo-coated chip exposed to five consecutive adsorption (green) and desorption (blue) cycles of aqueous 1 µM R6G solution pumped at 0.5 mL·min^{-1}. The inset exemplifies the SERS spectra for the fifth adsorption–desorption cycle. (b) Evolution of the Raman signal at 1516 cm^{-1}, recorded at a given position, during the first desorption stage carried out by flushing water through the microchannels.

Under similar conditions, the average SERS signal along the Au@PW microfluidic channel recorded on the first detection cycle is clearly superior to that of the Au@PMo counterpart, but also the RSD value (Figure S7 in the Supporting Information). In this case, a major fraction of R6G adsorbed during the first cycle was retained after the washing step (Figure 7b). This observation agrees with the strength of the interactions between the PW species and the dye molecules already described in the literature.[45] Although the reactivity of the outer PW shell might hinder the integration of Au@PW active regions in non-disposable sensing devices, it is

paving the way for a novel generation of single-use selective chips for SERS detection in real complex matrices.

Real time SERS Detection of Pesticides with Au@POM Microfluidic Devices

The remarkable results obtained with the organic dye prompted us to test the suitability of our Au@POM–coated chips in practical applications. We attempted the continuous detection of the organophosphorous paraoxon-methyl in aqueous solution 1 μM (0.275 mg·L^{-1}), as representative of the largest group of chemical insecticides globally used in crop protection. The lethal concentration (LC50) values of Paraoxon-methyl as reported in Daphnia magna (a small planktonic crustacean base of the food chain) are 233 and 2.33 μg L^{-1} after 1 h and 24 h, respectively.[46] The established WHO (World Health Organization) guidelines for the quality of drinking water regarding the presence of pesticides vary from 100 to 0.03 μg·L^{-1}.[47] SERS constitutes a promising and easier alternative to the standard chromatographic methods of pesticides detection.[48] The limit of detection (LOD) for pesticides is generally reported in the parts-per-million (ppm) or parts-per-billion (ppb) level, mainly as a result of advances in substrate development. However, the reproducibility of results becomes an issue for routine high throughput analysis in environmental samples, where only low cost and large SERS substrates are affordable.

Figure 8a shows the comparison of the recorded SERS spectra with the Raman spectrum of pure Paraoxon-methyl. The main characteristic absorption bands of the pesticide (Figure S8 and Table S2 in the Supporting Information) undergo slight blue shift upon interaction with the Au@POM substrates. Thus, the signal originating from the symmetric stretching vibration of the NO$_2$ group shifts from 1346 to 1365 cm^{-1} in our SERS spectra; and, that associated with the

vibration of the phenyl ring is displaced from 1590 cm^{-1} for the pure analyte to 1600 cm^{-1} due to the interactions with the POM shell as further explained with Figure 8b.

In close analogy to the R6G results, the SERS response of the Au@PW–coated chip is clearly superior to that of the Au@PMo counterpart for the Paraoxon-methyl detection. Once again, the Au-PW-adsorbate charge transfer contributes more effectively to the final SERS response. The spatial uniformity of the pesticide SERS signal along the microfluidic channel was also assessed by means of the average value and relative standard deviation (RSD) for the SERS intensity of the peak displayed at 1365 cm^{-1} recorded over a centimeter scale area of the substrate (100 random spots). The values so-obtained during the first cycle were 393 ± 21 cts·mW^{-1}·s^{-1} and 1368 ± 369 cts·mW^{-1}·s^{-1} for the Au@PMo and Au@PW devices, respectively. The averaged data of the Au@PMo chip results in a low RSD value, <7% which is considerably reliable for SERS measurements.[48] The theoretical limit of detection (LOD) is calculated as three times the noise level. From the noise signal of the above mentioned data set, *i.e.* 31·and 76 cts·mW^{-1}·s^{-1} for the Au@PMo and Au@PW devices; the LOD accounts for 2.11×10^{-7} M (52.1 µg·L^{-1}) and 1.67×10^{-7} M (41.4 µg·L^{-1}) for Au@PMo and Au@PW chips, respectively.
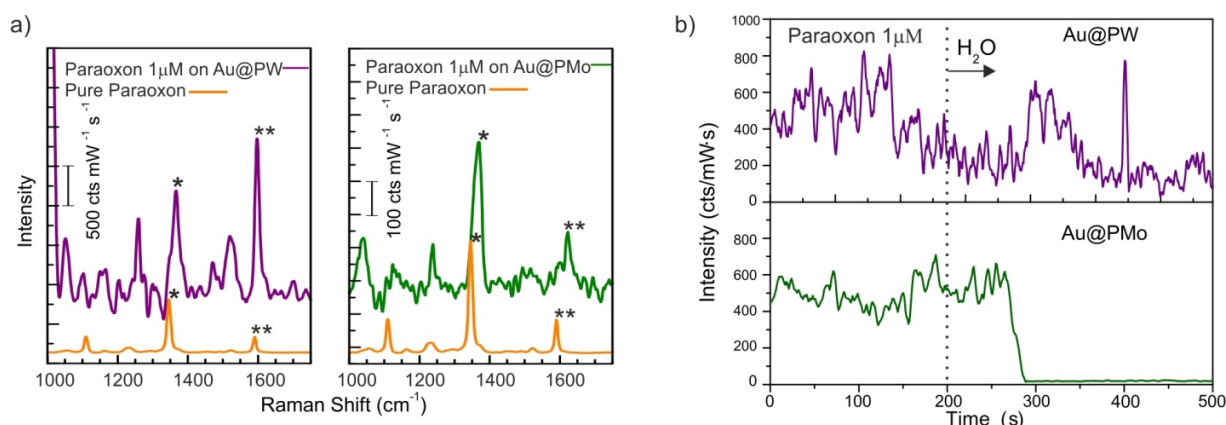
Figure 8. Continuous detection of an aqueous 1 µM Paraoxon-methyl solution pumped at 0.5 mL·min^{-1} through the LoC SERS devices. (a) SERS spectra for the Au@PW (left) and Au@PMo (right) nanostructures; * denotes the symmetric stretching vibration of the NO$_2$ group; ** denotes the stretching vibration of the phenyl ring. (b) Evolution of the Raman signal at 1365 cm^{-1}, recorded at a given position, during the first desorption stage carried out by flushing water through the microchannels.

As shown in Figure 8b, the adsorption of Paraoxon-methyl at the Au@PMo substrate is fully reversible and the device can be completely recovered for subsequent SERS experiments in less than 2 min by flushing distilled water. Thus, the Au@PMo–coated chip could be reused for the SERS detection of Paraoxon-methyl throughout at least three consecutive adsorption-desorption cycles without any significant loss of the signal intensity (Figure S7 in the Supporting Information).

In contrast to Au@PMo, the Au@PW substrate displays irreversible adsorption of Paraoxon-methyl in close analogy with R6G results. Detailed inspection of the shift of the spectral bands and the ratio between their intensities affords information about the analyte-surface bonding mechanism. In the case of the Au@PW substrate, the strong interaction between Paraoxon-methyl and the PW cluster shell would take place mainly through the phenyl ring. Aromatic-POM interactions involving π-electron-deficient rings have been well established in the literature,[49] and their occurrence indicates that the Au@PW substrate could be envisioned for developing microfluidic devices that couple the SERS detection of organophosphate compounds with their catalytic degradation.[50-51] The results discussed above highlight the significance of the POM shell in the performance of the SERS-active substrates fabricated in this work and open a number of possibilities of tunable properties by changing the nature of the POM cluster.

CONCLUSIONS

Two types of microfluidic devices based on Au@PMo or AuPW nanostructures (~100 nm in size) have been successfully fabricated, characterized and demonstrated for real time detection of paraoxon-methyl at micromolar range in synthetic samples. Our fabrication method provides a straightforward, simple, versatile and low cost route for in-situ integration of large SERS-active regions in microfluidic devices. The protective POM shell not only contributes to enhance the SERS enhancement factor by the charge transfer mechanism but also has advantages especially in analyte capture due to the unique reactivity of the metal –oxygen anionic clusters.

The so obtained Au@POM chips show a remarkable spatial uniformity of the SERS response and can be employed efficiently in SERS, i.e. AEF for R6G up to 1.65×10^7; similarly to Au based LoC-SERS prepared by other more sophisticated approaches. This fact contributes to the development of low-cost LoC-SERS systems for high throughput analysis in practical applications. The preliminary SERS detection results of organophosphorous pesticides in dynamic conditions reveal adequate for considering in quality monitoring of drinking water. Depending on the nature of the stabilizing POM shell, either single-use selective SERS chips (Au@PW) or reusable ones (Au@PMo) are straightforward obtained. Overall, the prospect of these LoC-SERS as alternative detection systems for water pollutants seems feasible.

ASSOCIATED CONTENT

Supporting Information

The Supporting Information is available free of charge on the ACS Publications website at DOI: 10.1021/acsami.XXXXXXX

Experimental set-up for the UV-light-driven synthesis of Au@POM nanostructures (Figure S1); Experimental set-up for the SERS detection experiments (Figure S2); Molecular structure of the PMo and PW anions (Figure S3); XPS analyses of the O1s core level of Au@POM structures (Figure S4); Characterization of the colloidal Au@POM nanoparticles collected from the outlet solution (Figure S5); Evolution of the Raman signal of R6G peak displayed at 1540 cm^{-1} measured at steady state conditions along 1200 μm on the central microfluidic channel of Au@POM coated chips (Figure S6); Evolution of the Raman signal measured on the Au@POM-coated chips exposed to consecutive adsorption-desorption cycles of aqueous 1 μM Paraoxon-methyl and R6G (Figure S7); Raman spectrum of Paraoxon-methyl (Figure S8); Experimental conditions of the SERS measurements (Table S1); Main specific Raman absorption bands for Paraoxon-methyl (Table S2) (PDF)

AUTHOR INFORMATION

Corresponding Author

*E–mail: mapina@unizar.es (M.P.P.)

*E–mail: santiago.reinoso@unavarra.es (S.R.)

ORCID

Marta Lafuente: 0000-0003-2660-3726

Ismael Pellejero: 0000-0002-8448-7543

Alberto Clemente: 0000-0002-8787-117X

Miguel A. Urbiztondo: 0000-0002-4931-1358

Reyes Mallada: 0000-0002-4758-9380

María P. Pina: 0000-0001-9897-6527

Santiago Reinoso: 0000-0001-8329-5972

Luis M. Gandía: 0000-0002-3954-4609

Author Contributions

The manuscript was written through contributions of all authors. All authors have given approval to the final version of the manuscript.

Notes

The authors declare no competing financial interests.

REFERENCES

(1) Alvarez-Puebla, R. A.; Liz-Marzán, L. M. Traps and Cages for Universal SERS Detection. *Chem. Soc. Rev.*, **2012**, *41*, 43-51.

(2) Sharma, B.; Frontiera, R. R.; Henry, A.-I.; Ringe, E.; Van Duyne, R. P. SERS: Materials, Applications, and the Future. *Mater. Today*, **2012**, *15*, 16-25.

(3) Shin, K. S.; Lee, H. S.; Joo, S. W.; Kim, K. Surface-Induced Photoreduction of 4-Nitrobenzenethiol on Cu Revealed by Surface-Enhanced Raman Scattering Spectroscopy. *J. Phys. Chem. C*, **2007**, *111*, 15223-15227.

(4) Chen, L. Y.; Yu, J. S.; Fujita, T.; Chen, M. W. Nanoporous Copper with Tunable Nanoporosity for SERS Applications. *Advanced Functional Materials*, **2009**, *19*, 1221-1226.

(5) Khaing Oo, M. K.; Chang, C.-F.; Sun, Y.; Fan, X. Rapid, Sensitive DNT Vapor Detection with UV-Assisted Photo-chemically Synthesized Gold Nanoparticle SERS Substrates. *Analyst*, **2011**, *136*, 2811-2817.

(6) Lu, G.; Li, H.; Liusman, C.; Yin, Z. Y.; Wu, S. X.; Zhang, H. Surface Enhanced Raman Scattering of Ag or Au Nanoparticle-Decorated Reduced Graphene Oxide for Detection of Aromatic Molecules. *Chem. Sci.*, **2011**, *2*, 1817-1821.

(7) Zhao, Y.; Yang, X.; Li, H.; Luo, Y. D.; Yu, R. P.; Zhang, L. L.; Yang, Y. X.; Song, Q. J. Au Nanoflower-Ag Nanoparticle Assembled SERS-Active Substrates for Sensitive MC-LR Detection. *Chem. Commun.*, **2015**, *51*, 16908-16911.

(8) Mandal, S.; Selvakannan, P.; Pasricha, R.; Sastry, M. Keggin Ions as UV-Switchable Reducing Agents in the Synthesis of Au Core-Ag Shell Nanoparticles. *J. Am. Chem. Soc.*, **2003**, *125*, 8440-8441.

(9) Troupis, A.; Hiskia, A.; Papaconstantinou, E. Synthesis of Metal Nanoparticles by Using Polyoxometalates as Photocatalysts and Stabilizers. *Angew. Chem.-Int. Edit.*, **2002**, *41*, 1911-1914.

(10) Wang, Y. F.; Weinstock, I. A. Polyoxometalate-Decorated Nanoparticles. *Chem. Soc. Rev.*, **2012**, *41*, 7479-7496.

(11) Mitchell, S. G.; de la Fuente, J. M. The Synergistic Behavior of Polyoxometalates and Metal Nanoparticles: from Synthetic Approaches to Functional Nanohybrid Materials. *J. Mater. Chem.*, **2012**, *22*, 18091-18100.

(12) Jameel, U.; Zhu, M.; Chen, X.; Tong, Z. Recent Progress of Synthesis and Applications in Polyoxometalate and Nanogold Hybrid Materials. *J. Mater. Sci.*, **2016**, *51*, 2181-2198.

(13) Liu, R. J.; Li, S. W.; Yu, X. L.; Zhang, G. J.; Ma, Y.; Yao, J. N.; Keita, B.; Nadjo, L. Polyoxometalate-Assisted Galvanic Replacement Synthesis of Silver Hierarchical Dendritic Structures. *Cryst. Growth Des.*, **2011**, *11*, 3424-3431.

(14) Pearson, A.; Bhosale, S.; Bhargava, S. K.; Bansal, V. Combining the UV-Switchability of Keggin Ions with a Galvanic Replacement Process to Fabricate TiO2-Polyoxometalate-Bimetal Nanocomposites for Improved Surface Enhanced Raman Scattering and Solar Light Photocatalysis. *ACS Appl. Mater. Interfaces*, **2013**, *5*, 7007-7013.

(15) Lai, Y.-H.; Chen, S.-W.; Hayashi, M.; Shiu, Y.-J.; Huang, C.-C.; Chuang, W.-T.; Su, C.-J.; Jeng, H.-C.; Chang, J.-W.; Lee, Y.-C.; Su, A.-C.; Mou, C.-Y.; Jeng, U.-S. Mesostructured Arrays of Nanometer-spaced Gold Nanoparticles for Ultrahigh Number Density of SERS Hot Spots. *Adv. Funct. Mater.*, **2014**, *24*, 2544-2552.

(16) Baruah, B.; Miller, T.-A. Polyoxovanadate Fabricated Gold Nanoparticles: Application in SERS. *J. Colloid Interface Sci.*, **2017**, *487*, 209-216.

(17) Zhou, Q.; Kim, T. Review of Microfluidic Approaches for Surface-Enhanced Raman Scattering. *Sens. Actuator B-Chem.*, **2016**, *227*, 504-514.

(18) Jahn, I. J.; Zukovskaja, O.; Zheng, X.-S.; Weber, K.; Bocklitz, T. W.; Cialla-May, D.; Popp, J. Surface-Enhanced Raman Spectroscopy and Microfluidic Platforms: Challenges, Solutions and Potential Applications. *Analyst*, **2017**, *142*, 1022-1047.

(19) Huang, J.-A.; Zhang, Y.-L.; Ding, H.; Sun, H.-B. SERS-Enabled Lab-on-a-Chip Systems. *Adv. Opt. Mater.*, **2015**, *3*, 618-633.

(20) Mao, H.; Wu, W.; She, D.; Sun, G.; Lv, P.; Xu, J. Microfluidic Surface-Enhanced Raman Scattering Sensors Based on Nanopillar Forests Realized by an Oxygen-Plasma-Stripping-of-Photoresist Technique. *Small*, **2014**, *10*, 127-134.

(21) Xu, B.-B.; Zhang, R.; Liu, X.-Q.; Wang, H.; Zhang, Y.-L.; Jiang, H.-B.; Wang, L.; Ma, Z.-C.; Ku, J.-F.; Xiao, F.-S.; Sun, H.-B. On-Chip Fabrication of Silver Microflower Arrays as a Catalytic Microreactor for Allowing In Situ SERS Monitoring. *Chem. Commun.*, **2012**, *48*, 1680-1682.

(22) Habermehl, A.; Strobel, N.; Eckstein, R.; Bolse, N.; Mertens, A.; Hernandez-Sosa, G.; Eschenbaum, C.; Lemmer, U. Lab-on-Chip, Surface-Enhanced Raman Analysis by Aerosol Jet Printing and Roll-to-Roll Hot Embossing. *Sensors*, **2017**, *17*, 2401.

(23) Lee, M. R.; Lee, H. K.; Yang, Y.; Koh, C. S. L.; Lay, C. L.; Lee, Y. H.; Phang, I. Y.; Ling, X. Y. Direct Metal Writing and Precise Positioning of Gold Nanoparticles within Microfluidic Channels for SERS Sensing of Gaseous Analytes. *ACS Appl. Mater. Interfaces*, **2017**, *9*, 39584-39593.

(24) Amin, R.; Knowlton, S.; Hart, A.; Yenilmez, B.; Ghaderinezhad, F.; Katebifar, S.; Messina, M.; Khademhosseini, A.; Tasoglu, S. 3D-Printed Microfluidic Devices. *Biofabrication*, **2016**, *8*, 022001.

(25) Bhattacharjee, N.; Urrios, A.; Kanga, S.; Folch, A. The Upcoming 3D-Printing Revolution in Microfluidics. *Lab Chip*, **2016**, *16*, 1720-1742.

(26) Yazdi, A. A.; Popma, A.; Wong, W.; Tammy, N.; Pan, Y.; Xu, J. 3D Printing: an Emerging Tool for Novel Microfluidics and Lab-on-a-Chip Applications. *Microfluid. Nanofluid.*, **2016**, *20*, 50.

(27) Fortuni, B.; Inose, T.; Uezono, S.; Toyouchi, S.; Umemoto, K.; Sekine, S.; Fujita, Y.; Ricci, M.; Lu, G.; Masuhara, A.; Hutchison, J. A.; Latterini, L.; Uji-i, H. In Situ Synthesis of Au-Shelled Ag Nanoparticles on PDMS for Flexible, Long-life, and Broad Spectrum-Sensitive SERS Substrates. *Chem. Commun.*, **2017**, *53*, 11298-11301.

(28) Lu, G.; Li, H.; Zhang, H. Nanoparticle-Coated PDMS Eelastomers for Enhancement of Raman Scattering. *Chem. Commun.*, **2011**, *47*, 8560-8562.

(29) Park, S.; Lee, J.; Ko, H. Transparent and Flexible Surface-Enhanced Raman Scattering (SERS) Sensors Based on Gold Nanostar Arrays Embedded in Silicon Rubber Film. *ACS Appl. Mater. Interfaces*, **2017**, *9*, 44088-44095.

(30) Castedo, A.; Mendoza, E.; Angurell, I.; Llorca, J. Silicone Microreactors for the Photocatalytic Generation of Hydrogen. *Catal. Today*, **2016**, *273*, 106-111.

(31) Tebandeke, E.; Coman, C.; Guillois, K.; Canning, G.; Ataman, E.; Knudsen, J.; Wallenberg, L. R.; Ssekaalo, H.; Schnadt, J.; Wendt, O. F. Epoxidation of Olefins with Molecular Oxygen as the Oxidant Using Gold Catalysts Supported on Polyoxometalates. *Green Chem.*, **2014**, *16*, 1586-1593.

(32) Kyndiah, A.; Ablat, A.; Guyot-Reeb, S.; Schultz, T.; Zu, F.; Koch, N.; Amsalem, P.; Chiodini, S.; Yilmaz Alic, T.; Topal, Y.; Kus, M.; Hirsch, L.; Fasquel, S.; Abbas, M. A Multifunctional Interlayer for Solution Processed High Performance Indium Oxide Transistors. *Sci. Rep.*, **2018**, *8*, 10946.

(33) Kozhevnikov, I. V. Catalysis by Heteropoly Acids and Multicomponent Polyoxometalates in Liquid-Phase Reactions. *Chem. Rev.*, **1998**, *98*, 171-198.

(34) Maestre, J. M.; Lopez, X.; Bo, C.; Poblet, J.-M.; Casañ-Pastor, N. Electronic and Magnetic Properties of α-Keggin Anions: A DFT Study of $[XM_{12}O_{40}]^{n-}$, (M = W, Mo; X = Al^{III}, Si^{IV}, P^V, Fe^{III}, Co^{II}, Co^{III}) and $[SiM_{11}VO_{40}]^{m-}$ (M = Mo and W). *J. Am. Chem. Soc.*, **2001**, *123*, 3749-3758.

(35) De Vera, J. S.; Venault, A.; Chou, Y.-N.; Tayo, L.; Chiang, H.-C.; Aimar, P.; Chang, Y. Self-Cleaning Interfaces of Polydimethylsiloxane Grafted with pH-Responsive Zwitterionic Copolymers. *Langmuir*, **2019**, *35*, 1357-1368.

(36) Kozhevnikov, I. V. Advances in the Catalysis by Heteropoly-Acids. *Uspekhi Khimii*, **1987**, *56*, 1417-1443.

(37) M. Lafuente; I. Pellejero; V. Sebastián; Urbiztondo, M. A.; R.Mallada; Pina, M. P.; Santamaría, J. Highly Sensitive SERS Quantification of Organophosphorous Chemical Warfare Agents: a Major Step Towards the Real Time Sensing in the Gas Phase. *Sens. Actuator B-Chem.*, **2018**, *267*, 457-466.

(38) Alvarez-Puebla, R. A. Effects of the Excitation Wavelength on the SERS Spectrum. *J. Phys. Chem. Lett.*, **2012**, *3*, 857-866.

(39) Bridgeman, A. J. Computational Study of the Vibrational Spectra of alpha- and beta-Keggin Polyoxometalates. *Chem.-Eur. J.*, **2004**, *10*, 2935-2941.

(40) Lica, G. C.; Browne, K. P.; Tong, Y. Interactions between Keggin-Type Lacunary Polyoxometalates and Ag Nanoparticles: A Surface-Enhanced Raman Scattering Spectroscopic Investigation. *J. Clust. Sci.*, **2006**, *17*, 349-359.

(41) Xu, M.; Liu, C.; Xu, Y.; Li, W.; Wu, L. Incorporation of Metal Nanoparticles into H3PMo12O40 Hybrid Langmuir-Blodgett Film through In-situ Reduction. *Colloids Surf. A*, **2009**, *333*, 46-52.

(42) Lafuente, M.; Berenschot, E. J. W.; Tiggelaar, R. M.; Mallada, R.; Tas, N. R.; Pina, M. P. 3D Fractals as SERS Active Platforms: Preparation and Evaluation for Gas Phase Detection of G-Nerve Agents. *Micromachines*, **2018**, *9*, 60.

(43) Stiles, P. L.; Dieringer, J. A.; Shah, N. C.; Van Duyne, R. R. Surface-Enhanced Raman Spectroscopy. *Annu. Rev. Anal. Chem.*, **2008**, *1*, 601-626.

(44) Moore, J. E.; Morton, S. M.; Jensen, L. Importance of Correctly Describing Charge-Transfer Excitations for Understanding the Chemical Effect in SERS. *J. Phys. Chem. Lett.*, **2012**, *3*, 2470-2475.

(45) Zhu, T.-T.; Zhang, Z.-M.; Chen, W.-L.; Liu, Z.-J.; Wang, E.-B. Encapsulation of Tungstophosphoric Acid into Harmless MIL-101(Fe) for Effectively Removing Cationic Dye from Aqueous Solution. *RSC Adv.*, **2016**, *6*, 81622-81630.

(46) Duquesne, S.; Reynaldi, S.; Liess, M. Effects of the Organophosphate Paraoxon-methyl on Survival and Reproduction of Daphnia Magna: Importance of Exposure Duration and Recovery. *Environ. Toxicol. Chem.*, **2006**, *25*, 1196-1199.

(47) Organization, W. H., *Guidelines for drinking-water quality, 4th edition, incorporating the 1st addendum*, World Health Organization, 4th edition edn., 2017.

(48) Pang, S. T. R.; Yang, T. X.; He, L. L. Review of Surface Enhanced Raman Spectroscopic (SERS) Detection of Synthetic Chemical Pesticides. *Trac-Trends Anal. Chem.*, **2016**, *85*, 73-82.

(49) Reinoso, S.; Vitoria, P.; Felices, L. S.; Lezama, L.; Gutierrez-Zorrilla, J. M. Analysis of Weak Interactions in the Crystal Packing of Inorganic Metalorganic Hybrids Based on Keggin

Polyoxometalates and Dinuclear Copper(II)-acetate Complexes. *Inorg. Chem.*, **2006**, *45*, 108-118.

(50) Mizrahi, D. M.; Saphier, S.; Columbus, I. Efficient Heterogeneous and Environmentally Friendly Degradation of Nerve Agents on a Tungsten-Based POM. *J. Hazard. Mater.*, **2010**, *179*, 495-499.

(51) Kaledin, A. L.; Troya, D.; Karwacki, C. J.; Balboa, A.; Gordon, W. O.; Morris, J. R.; Mitchell, M. B.; Frenkel, A. I.; Hill, C. L.; Musaev, D. G. Key Mechanistic Details of Paraoxon Decomposition by Polyoxometalates: Critical Role of para-Nitro Substitution. *Chem. Phys.*, **2019**, *518*, 30-37.

For Table of Contents Only